Research Square

Preprints are preliminary reports that have not undergone peer review.
They should not be considered conclusive, used to inform clinical practice,
or referenced by the media as validated information.

Quantitative Sensitivity Analysis of Hybrid Nanofluid Transport over a Convective Rotating Stretchable Disk with Variable Thermophysical Properties and chemical reaction

Muhammad Ramzan
Imam Mohammad ibn Saud Islamic University
Hamna Nazir
The University of Chenab, Gujrat
Muhammad Bilal
me.bilal.786@gmail.com

The University of Chenab, Gujrat
Tanveer Sajid
University of Lahore
Adil Jhangeer
VSB - Technical University of Ostrava
Yasir Mehmood
The University of Lahore, Sargodha Campus
Yazeed Alkhrijah
Imam Mohammad ibn Saud Islamic University
Koh Wei Sin
INTI International University

Research Article

Keywords: Stretching disk, hybrid nanofluid, energy efficiency, sensitivity and tornado analysis, variable viscosity

Posted Date: August 5th, 2026

DOI: https://doi.org/10.21203/rs.3.rs-10444534/v1

License: This work is licensed under a Creative Commons Attribution 4.0 International License.
Read Full License

Additional Declarations: No competing interests reported.

Quantitative Sensitivity Analysis of Hybrid Nanofluid Transport over a Convective Rotating Stretchable Disk with Variable Thermophysical Properties and chemical reaction

Muhammad Ramzan[1], Hamna Nazir[2], Muhammad Bilal[2,a], Tanveer Sajid[3], Adil Jhangeer[4,5,6], Yasir Mehmood[7], Yazeed Alkhrijah[1], Koh Wei Sin[8]

1. Department of Mathematics and Statistics, College of Science, Imam Mohammad Ibn Saud Islamic University (IMSIU), Riyadh 13318, Saudi Arabia

2. Department of Physical Sciences, The University of Chenab, Gujrat, Pakistan

3. International Centre for Interdisciplinary Research in Sciences, The University of Lahore, Lahore, Pakistan

4. IT4-Innovations, VSB- Technical University of Ostrava, Ostrava-Poruba, Czech Republic

5. Center for Theoretical Physics, Khazar University, 41 Mehseti Str., Baku, AZ1096, Azerbaijan

6. Department of Computer Engineering, Biruni University, Istanbul, Turkey.

7. Department of Mathematics, The University of Lahore, Sargodha Campus, Pakistan

8. Department of Electrical Engineering, College of Engineering, Imam Mohammad Ibn Saud Islamic University (IMSIU), Riyadh 13318, Saudi Arabia

9. Inti International University, Persiaran Perdana BBN, Putra Nilai, 71800 Nilai, Negeri Sembilan, Malaysia

a. Corresponding author e-mail address: me.bilal.786@gmail.com

Abstract: The present study investigates the enhancement of thermal energy transfer in a hybrid nanofluid flow driven by a spinning and stretching Riga disk, incorporating the effects of chemical reactions and thermal radiation. The thermal performance is evaluated using silver and aluminum oxide nanoparticles dispersed in a water-based fluid. To increase the physical realism, the Darcy-Forchheimer model is applied to capture internal and porous media effects. Temperature-dependent viscosity and thermal conductivity are considered alongside a convective temperature boundary condition and a zero mass flux constraint. In addition to conventional velocity, temperature, and concentration analysis, a comprehensive sensitivity framework based on perturbation theory and tornado visualization is developed to quantitatively identify the dominant transport mechanisms governing heat and mass transfer characteristics. Scaling group transformations reduce the governing partial differential equations to a system of ordinary differential equations, which are then solved numerically using MATLAB's bvp4c method. The thermophysical properties of the hybrid nanofluid are further analyzed through the Levenberg-Marquardt back-propagation technique. According to the sensitivity analysis, mass transport behavior is mostly dominated by

Brownian motion and thermophoretic effects, whereas the Biot number has the greatest impact on the Nusselt number. The suggested approach greatly improves the interpretability and prediction power of nonlinear nanofluid transport systems and offers a clear hierarchy of regulating physical factors.

Keywords: Stretching disk; hybrid nanofluid; energy efficiency; sensitivity and tornado analysis; variable viscosity

Nomenclature

$B_i's$	dimensionless constants	v	Kinematic viscosity $\left(m^2/s\right)$
$k_\circ$	Permeability of porous medium $\left(m^2\right)$	$F_\circ$	Porous medium coefficient
C_b	Drag force coefficient	σ	Electrical conductivity (S/m)
ρ	Density $\left(kg/m^3\right)$	$B_\circ$	Magnetic field strength (T)
$M_\circ$	Riga plate (external) magnetic field strength (T)	$j_\circ$	Current density $\left(A/m^2\right)$
$a_\circ$	Riga plate constant	T	Temperature (K)
k	Thermal conductivity $(W/m\ K)$	σ^*	Stefan- Boltzmann constant
s	Shape factor	T_∞	Ambient temperature (K)
k^*	Absorption coefficient $(1/m)$	c_p	Specific heat $(J/\left(kg\ K\right))$
T_f	Disc temperature (K)	$Q_\circ$	Heat source (J)
μ	Dynamic viscosity $(kg/\left(ms\right))$	D_B	Brownian diffusion coefficient
C	Concentration $\left(kg/m^3\right)$	Br	Brinkman number
N_t	Thermophoresis parameter	k_r^2	Chemical reaction rate constant
ω	Constant angular velocity (R/s)	η	Similarity transformation coordinate
θ	Dimensionless temperature	ϕ	Dimensionless concentration
F'	Dimensionless radial velocity	G	Dimensionless tangential velocity
ϕ_1	Volume fraction of Al_2O_3	ϕ_2	Volume fraction of Ag
Nu	Nusselt number	Pr	Prandtl number
Ec	Eckert number	C_p	coefficient of skin friction
β	Porosity parameter	Sh	Sherwood number
Fr	Darcy-Forchheimer parameter	Ha	Hartmann number
Rd	Radiation parameter	D_T	Thermophoretic diffusion coefficient
γ	Width parameter	N_b	Brownian motion parameter
C_∞	Ambient concentration $\left(kg/m^3\right)$	Sc	Schmidt number
Kr	Chemical reaction parameter	M	Magnetic parameter
λ	Suction-injection parameter	α	variable viscosity

1 Introduction

Among the most significant problems in fluid mechanics, with a broad range of scientific and engineering applications, is fluid flow over a revolving disk. Depending on the context, its applications can range from energy extraction and drag reduction to mixing optimization, improved

heat transfer, and increasing efficiency of scientific devices. Flows over a rotating disk find applications in swirl coating, centrifugal machinery, high temperature metal pumping, and turbo machinery in scientific and geophysical systems. Von Karman [1] was the first to study the flow on a spinning disk. He proposed the transformations that reduced the Navier-Stokes equations to the momentum integral, and a set of regular differential equations. Berker [2, 3] later found that whenever two infinite parallel plane plates are spinning around the same or different axes, there are endless enumerate of non-trivial solutions to the Navier-Stokes equations. He assumed a single solution symmetric about the origin. In this particular kind of flow, non-Newtonian fluids have also been looked at. Raju et al. [4] examined the nonlinear convective surface radiation flow of magnesium oxide nanoparticles containing nanofluids over a disk that rotates. They found that the convection coefficient mixture of ethylene glycol and magnesium oxide is higher than that of a combination of water and Mg oxide because of nonlinear temperature fluctuation in motion. This scenario was initially tackled by Bodewadt [5], who, using energetic analysis, expressed that near the disk, fluid flows radially inward with an even velocity, balanced by axial outflow such that mass continuity is preserved. The behavior of the non-Newtonian Casson methanol-based $AA7072$ nanofluid in a complex flow situation was thoroughly investigated by Ragupathi et al. [6]. Their work investigated how the magnetic dipole interaction affects rotating disks. They also studied the impact of Joule heating to discuss the combined influences of electromagnetic and thermal conduction forces on the fluid mechanics. Mehmood et al. [7] analyzed an in-depth study of MHD flow behavior of a nanofluid concocted with unique carbon nanotubes (CNTs) dispersed in engine oil. The study includes the effect of chemical reactions pertaining to the flow dynamics across the stretched and rotating disk. It turned out that the rise in nanoparticles concentration favors the skin friction coefficient and Nusselt number during the heat transfer. Chen et al. [8] contributed valuable insights into radially stretchable porous rotating disks by validating numerical models experimentally. The study strongly emphasized the need for precise characterization of deformation patterns and inherent porous properties of the disks to improve the predictability of their mechanical and flow behavior. The experimental findings reveal a complex relationship between material porosity, radial stretching, and rotational dynamics that provides significant new insights into their interactive influence. In order to improve the melting phenomena in a spinning disk impacted by externally applied pressure, Taghavi [9] conducted a thorough analysis. The study merely notes that the melting rate was significantly increased by both the combined impact of rotation and applied pressure. Attia [10] investigated how a magnetic field affected unsteady flow across a revolving disk that was permeable and applicable to both injection and suction at its surface. Because of the greater contact among the injecting fluid and the magnetic forces, he observed that the effects of the magnetic field on the flow dynamics were stronger under injection than under suction phenomenon. Rashidi et al. [11] evolved analytical results for steady flow driven by a rotating disk in a porous substance, along with the related heat transfer phenomena. Their work focused on assessing complex interactions among the rotation-induced flow, the porous medium structure, and the transfer of thermal energy. Yaseen et al. [12] looked into the radiative motion of a kerosene oil-based nanoliquid flowing between two rotating disks in detail. They examined both porous medium and inertial effects through the Darcy-Forchheimer model.

Ramzan et al. [13] conducted a comparative study on the thermal convection in a non-aging hybrid nanofluid containing various types of nanoparticles, stirred between two rotating disks. Their results indicate that the degree of temperature alteration of the fluid varies due to the interfering phenomena of radiation and thermal stratification. Ram et al. [14] studied the magneto-viscous effects in a nanofluid with magnetic nanoparticles infused in it under the weakly oscillating magnetic field over a rotary disk. Their work focused on how the magnetic field altered the velocity contours and temperature distributions in the ferrofluid, enhancing understanding of its motion and heating behavior.

Hybrid nanofluids consist of suspensions of two or more distinct kinds of nanoparticles either in the same or different base fluids to enhance their thermal and mechanical properties, thereby improving the heat transfer efficiency in diverse applications. One of the major application of hybrid nanofluids is in the cooling of the automobile radiator, where their superior heat transfer performance assures engine cooling efficiency, fuel consumption reduction, and improved overall vehicle performance. Owing to these benefits, hybrid nanofluids are gaining ever increasing attention in industrial and engineering domains. A detailed analysis was made on the hybrid nanofluid characteristics within a viscous fluid's path around the rotating surface; Acharya et al. [15] have done commendable work, understanding how a mixture of different nanoparticles will dramatically change the behavior of the said fluid in along with its heat transfer properties. A computational evaluation was conducted by Rahman et al. [16] to explore the features of the hybrid nanofluid consisting of Al_2O_3 and Cu nanoparticles suspended in H_2O, focusing on forced convection in an axisymmetric tube. Their results demonstrated that, in contrast to a typical fluid, the presence of particles suspended in it improves the nanofluid's capacity to transfer heat. Ahmad et al. [17] compared the thermodynamic behavior regarding the hybrid nanofluid ($Al_2O_3\&Cu/water$) with that of a convectional nanofluid ($water$) flowing through a porous medium while considering viscous dissipation effects. Their study examined how these fluids behaved when passing through a porous medium that accounts for viscous dissipation that is, internal heat generation from friction and examined how these factors affected heat exchange and flow patterns over an extended surface. Ghadikolaei et al. [18] studied the flow of a Carreau hybrid nanofluid over a rotating cone in the presence of magnetic field. This hybrid nanofluid consisted of ethylene glycol with the suspension of titanium oxide (TiO_2) and copper oxide (CuO) nanoparticles. Tayari et al. [19] employed the collocation method to simulate hybrid nanofluids flow over a flat plate. They surveyed that increasing the concentration of hybrid nanotubes in the fluid, thinned the thermal and velocity boundary layers, thereby enhancing heat and momentum transfer. Chamkha et al. [20] examined the transmission of heat occurrence as an outcome of the magnetohydrodynamic movement of a hybrid nanofluid across the moving disk sustained between the two parallel plates, considering Joule heating and thermal radiation. Khan et al. [21] used the two phase mixed hybrid nanofluid model to study the entropy generation and hydrothermal performance through collector and bent-plate. In a solar-powered spacecraft, Shaheen et al. [22] investigated hybrid nanofluid flow over an inclined surface that was either stretching or contracting. They upgraded heat transfer and optimize entropy generation with very small copper (Cu) and alumina (Al_2O_3) nanoparticles dis-

persed in water. Aworinde et al. [23] considered the influence of a Riga plate on the steady circulation of a Casson hybrid nanofluid nearby a stretching cylinder in a porous medium with additional heating and thermal radiation. In order to account for Brownian movement and thermophoresis, Ferdows et al. [24] investigated the rheological properties of a nanofluid composed of a hybrid nanofluid comprising $(Cu-Al_2O_3-water)$, moved over a stretched or contracting surface.

Variable thermal conductivity is a property of materials to change its thermal conductivity that vary with temperature, composition, or other external influences. Unlike materials with constant thermal conductivity, whose thermal behavior kept constant under such constraints, variable thermal conductivity can altered with varying circumstances. This dynamic behavior is of utmost importance for enabling the transfer of heat to be efficient in many applications. Such behavior underpins cooling electronics and automobiles systems with nanofluids, protects spacecraft and high-speed aircraft in aerospace thermal-protection systems, and enhances phase-change materials used for energy storage. Hayat et al. [25] performed research within the context of mixed convection elastic viscous movement of fluid across a stretched pipe having an uneven source of heat and varying thermal conductivity. Choudhury and Hazarika [26] scrutinized MHD stagnation point flow while taking thermal conductivity and variable viscosity into account. The impact of both steady and changing conductivity of heat with the absorption heat generation over the Williamson fluid flow across an expanding cylinder was interrogated by Malik et al. [27]. An entropy generation study on the fluid flow over the exponentially stretching sheet, describing a variable thermal conductivity and viscosity, has been addressed by Afridi et al. [28]. The study explored how these variations relate to the irreversibility of the system and hence affect the energy efficiency and heat transfer. Sowmya and Gireesha [29] considered a porous radial fin, accounting for temperature-dependent conductivity and radiation. Two examples were reviewed in which thermal conductivity continuously varies with temperature in either a linear or an exponential manner. In the study of Hamid et al. [30], the influence of various shapes of (MoS_2) nanoparticles on circulating nanofluid flow was assessed through a stretched plate, taking into account the influence of magnetohydrodynamics, variable thermal conductivity, and thermal radiation. The authors concluded that the heat transfer was most effective with the use of platelet-shaped MoS_2 nanoparticles. Ahmad et al. [31] endeavored the rheology of Oldroyd-B fluid over an accelerating, periodically moving sheet taking into consideration the Cattaneo-Christov model. They found that the influence of heat source parameters markedly enhance temperature. Lahmar et al. [32] observed the unsteady squeezing flow and heat transfer for $Fe_2O_3 - water$ nanofluid in the system of parallel plates having temperature-dependent conductivity exposed to an oblique magnetic field. Sultan et al. [33] analyzed how mixed convective magnetohydrodynamic flow pattern developed when a cross fluid moves across a bidirectional stretching sheet documenting how heat absorption/generation alongside varying thermal conductivity influences fluid flow and heat transfer characteristics. The purpose of the work of Waqas et al. [34] is to investigate 2-dimensional bio convectional Casson nanofluid flow across a wedge incorporating the gyrostatic microorganisms, thermal radiation, variable thermal conductivity, and activation energy. A model of an unsteady incompressible Sutterby fluid has been examined by Abbas et al. [35], whereby a comparison of flow

over a flexible cylinder and sheet is undertaken. The analysis incorporates an induced magnetic field with thermal slip, Darcy resistance, viscous dissipation, and variable thermal conductivity.

While hybrid nanofluid flows under different physical configurations have been studied in great detail, the combined effects of a spinning and stretching Riga disc, porous medium effects, thermal radiation, and chemical reactions in a hybrid nanofluid framework have not been sufficiently investigated. The temperature and flow behaviour of a water-based hybrid nanofluid made of silver Ag and aluminium oxide Al_2O_3 nanoparticles across a stretching and rotating Riga surface is examined in this work to close this gap. The model includes zero mass flux constraint, a convective thermal boundary condition, thermal conductivity and temperature-dependent viscosity, and porous medium resistance through the Darcy-Forchheimer model to improve physical realism. By using a strict sensitivity-based approach, the current work expands the research toward a deeper physical understanding, in contract to traditional studies that mainly concentrate on velocity, temperature and concentration profiles. Specifically, the impact of governing parameters on rate of heat transfer, momentum transport and mass transfer has been quantitatively ranked using a perturbation-based sensitivity analysis in conjunction with tornado diagram visualization. A key novelty of this study lies in identifying the dominant and negligible physical mechanism governing transport phenomena in a unified manner. The results reveal that thermal boundary conditions, represented by the Biot number, exert the strongest control over heat transfer performance, while nanoparticle dynamics such as Brownian and thermophoresis primarily govern mass transport behavior. Furthermore, magnetic effects are shown to have a secondary yet non-gegligible roel in modifying momentum transport. Overall, this study goes beyond classical parametric analysis by offering a predistive framework for parameter prioritization, thereby enhancing the interpretability, optimization potential, and physical insight of complex multiphase transport. The proposed methodology provides a valuable benchmark for further numerical and theoretical investigations in magnetized nanofluid flow.

2 Mathematical formulation

This research focuses on the qualitative thermal and mass transport features of pseudo plastic, electrically conducting, and incompressible hybrid nanofluid ($Ag - Al_2O_3/H_2O$) over a stretching and rotating disc which is embedded in a highly permeable medium. The setup includes a Riga plate convectively heated as shown in Figure 1, fitted with electrodes and aligned magnets, and accounts for thermal radiation, magnetohydrodynamics (MHD), viscous heating, and first order chemical reaction with rate constant k_r^2. The disc lies in the (r, ϕ) plane and rotates at angular speed ω whilst stretching radially and moving vertically at $U_w = r\omega$. A linear dependence of temperature is assumed for thermal conductivity, viscosity, and inflow within the convective boundary condition, along with a zero mass flux condition. The system encompasses non-trivial multidimensional complex coupling phenomena typical in sophisticated heat and fluid flow devices. The disc maintains a constant surface temperature T_w, whereas the ambient temperature is T_∞. A consistent $\overrightarrow{B} = (B_0, 0, 0)$ is directed along the z axis as shown in Fig. 2. Owing to the axial sym-

metry, changes in ϕ direction are ignored. The velocity constituents in the r, ϕ, and z directions are represented by the variables W, V, and U, respectively. The mathematical framework for the flow of fluids problem can be stated as follows under the above indicated assumptions [36, 37].

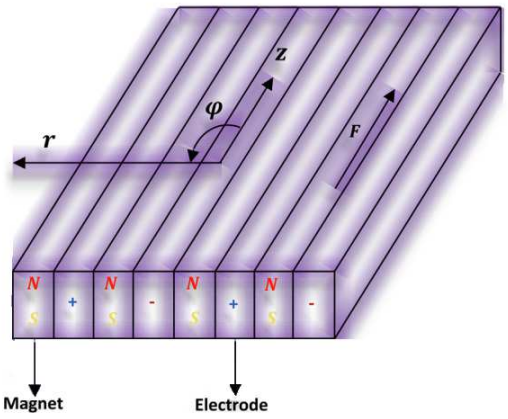


Figure 1: Geometric Setup of Riga Plate

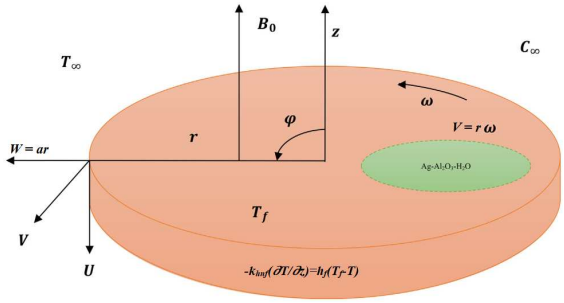


Figure 2: Physical Configuration of the Model

$$\frac{\partial W}{\partial r}+\frac{W}{r}+\frac{\partial U}{\partial z}=0, \tag{1}$$

$$W\frac{\partial W}{\partial r}-\frac{V^2}{r}+U\frac{\partial W}{\partial z}=\frac{1}{\rho_{hnf}}\frac{\partial}{\partial r}\left(-p+\mu_{hnf}\left(T\right)\left(\frac{\partial W}{\partial r}+\frac{W}{r}\right)\right)+$$
$$\frac{1}{\rho_{hnf}}\frac{\partial}{\partial z}\left(\mu_{hnf}\left(T\right)\frac{\partial W}{\partial z}\right)-\frac{\mu_{hnf}\left(T\right)}{\rho_{hnf}}\frac{W}{k_\circ}-F_\circ W^2+\frac{\pi}{8}\frac{j_\circ M_\circ}{\rho_{hnf}}e^{\left(-\frac{\pi}{a_\circ}\right)z}, \tag{2}$$

$$W\frac{\partial V}{\partial r}+\frac{V.W}{r}+U\frac{\partial V}{\partial z}=\frac{1}{\rho_{hnf}}\frac{\partial}{\partial r}\left(\mu_{hnf}\left(T\right)\left(\frac{\partial V}{\partial r}+\frac{V}{r}\right)\right)+\frac{1}{\rho_{hnf}}\frac{\partial}{\partial z}\left(\mu_{hnf}\left(T\right)\frac{\partial V}{\partial z}\right)$$
$$-\frac{\mu_{hnf}\left(T\right)}{\rho_{hnf}}\frac{V}{k_\circ}-F_\circ V^2+\frac{\pi}{8}\frac{j_\circ M_\circ}{\rho_{hnf}}e^{\left(-\frac{\pi}{a_\circ}\right)z}, \tag{3}$$

Properties	Notation	Nanoparticles		Base Fluid
		Ag	Al_2O_3	H_2O
Specific heat $(J/kg\ K)$	C_p	235	765	4179
Density (Kg/m^3)	ρ	10500	3970	997
Thermal conductivity (W/mK)	k	429	40	0.613

Table 1: The physical and thermal properties of hybrid nanofluids

$$W\frac{\partial T}{\partial r}+U\frac{\partial T}{\partial z}=5.333\frac{\sigma^{*}T_{\infty}^{3}}{k^{*}\left(\rho c_{p}\right)_{hnf}}\left(\frac{\partial^{2}T}{\partial z^{2}}+\frac{\partial^{2}T}{\partial r^{2}}+\frac{1}{r}\frac{\partial T}{\partial r}\right)+$$
$$\frac{1}{\left(\rho c_{p}\right)_{hnf}}\frac{\partial}{\partial r}\left(k_{hnf}\left(T\right)\frac{\partial T}{\partial r}\right)+\frac{1}{\left(\rho c_{p}\right)_{hnf}}\frac{k_{hnf}\left(T\right)}{r}\frac{\partial T}{\partial r}+\frac{1}{\left(\rho c_{p}\right)_{hnf}}\frac{\partial}{\partial z}\left(k_{hnf}\left(T\right)\frac{\partial T}{\partial z}\right)$$
$$+\frac{\pi}{8}\frac{j_{\circ}M_{\circ}}{\left(\rho c_{p}\right)_{hnf}}e^{\left(-\frac{\pi}{a_{\circ}}\right)z}\left(W+V\right)+\frac{\mu_{hnf}}{\left(\rho c_{p}\right)_{hnf}}\left(\left(\frac{\partial W}{\partial z}\right)^{2}+\left(\frac{\partial V}{\partial z}\right)^{2}\right)$$
$$+\tau\left(D_{B}\left(\frac{\partial T}{\partial r}\frac{\partial C}{\partial r}+\frac{\partial T}{\partial z}\frac{\partial C}{\partial z}\right)+\frac{D_{T}}{T_{\infty}}\left(\left(\frac{\partial T}{\partial r}\right)^{2}+\left(\frac{\partial T}{\partial z}\right)^{2}\right)\right), \tag{4}$$

$$W\frac{\partial C}{\partial r}+U\frac{\partial C}{\partial z}=D_{B}\left(\frac{1}{r}\frac{\partial C}{\partial r}+\frac{\partial^{2}C}{\partial z^{2}}+\frac{\partial^{2}C}{\partial r^{2}}\right)+\frac{D_{T}}{T_{\infty}}\left(\frac{\partial^{2}T}{\partial z^{2}}+\frac{\partial^{2}T}{\partial r^{2}}+\frac{1}{r}\frac{\partial T}{\partial r}\right)-$$
$$kr^{2}\left(C-C_{\infty}\right), \tag{5}$$

The conditions at the boundary associated with the mathematical formulation as follows,

$$\left.\begin{array}{llll} W=ar, \quad U=0, \quad V=r\omega, \quad D_{B}\dfrac{\partial C}{\partial z}+\left(\dfrac{D_{T}}{T_{\infty}}\right)\dfrac{\partial T}{\partial z}=0, \\ -k_{hnf}\dfrac{\partial T}{\partial z}=h_{f}\left(T_{f}-T\right) \quad \text{at} \quad z=0, \\ W\rightarrow 0, \quad V\rightarrow 0, \quad T\rightarrow T_{\infty}, \quad C\rightarrow C_{\infty} \quad \text{as} \quad z\rightarrow\infty, \end{array}\right\} \tag{6}$$

The flow of electricity per unit area, or current density $j_{\circ}$, is a crucial metric in nanofluid investigations. The motion of nanoparticles caused by random collisions is described by the Brownian diffusion coefficient D_B and temperature gradients by the thermophoretic diffusion coefficient D_T both of which are expressed in m/s. In relation to the base fluid, the dimensionless ratio τ indicates the effective heat capacity of the nanoparticle material, which effects the thermal behavior of the nanofluid. Recognizing heat and mass transmission in nanofluid systems requires an understanding of these characteristics. For the hybrid nanofluid, the terms ν_{hnf}, σ_{hnf}, and μ_{hnf} stand for its kinematic viscosity, electrical conductivity, and dynamic viscosity, respectively [36]. Table 1 lists the thermophysical characteristics that correlate to the chosen hybrid nanofluid and provides a mathematical definition. [36]

$$\frac{k_{hnf}}{k_{nf}} = \frac{k_2 + \phi_2 (1-s)(k_{nf} - k_2) - k_{nf}(1-s)}{k_2 + \phi_2 (k_{nf} - k_2) + k_{nf}(1-s)},$$

where$k_nf$is

$$\frac{k_{nf}}{k_f} = \frac{k_1 + \phi_1 (1-s)(k_f - k_1) - k_f (1-s)}{k_1 + \phi_1 (k_f - k_1) + k_f (1-s)},$$

$$\frac{\sigma_{hnf}}{\sigma_{nf}} = \frac{\sigma_2 + \phi_2 (1-s)(\sigma_{nf} - \sigma_2) - \sigma_{nf}(1-s)}{\sigma_2 + \phi_2 (\sigma_{nf} - \sigma_2) + \sigma_{nf}(1-s)},$$

where$\sigma_n f$is

$$\frac{\sigma_{nf}}{\sigma_f} = \frac{\sigma_1 + \phi_1 (1-s)(\sigma_f - \sigma_1) - \sigma_f (1-s)}{\sigma_1 + \phi_1 (\sigma_f - \sigma_1) + \sigma_f (1-s)},$$

$$\frac{\mu_{hnf}}{\mu_f} = [(1-\phi_1)(1-\phi_2)]^{-2.5},$$

$$\rho_{hnf} = [(1-\phi_1)\rho_f + \phi_1 \rho_1](1-\phi_2) + \phi_2 \rho_2,$$

$$(\rho c_p)_{hnf} = \left[(1-\phi_1)(\rho c_p)_f + \phi_1 (\rho c_p)_1\right](1-\phi_2) + \phi_2 (\rho c_p)_2,$$

A system of ODEs is created by reducing the system of PDEs (1)-(5) using the following sequence of transformations.

$$\left.\begin{array}{lll} W = r\omega F^{'}(\eta), & V = r\omega G(\eta), & U = -2\sqrt{\omega \upsilon_f} F(\eta) \\ \eta = \sqrt{\dfrac{\omega}{\upsilon_f}} z, & \theta(\eta) = \dfrac{T - T_\infty}{T_f - T_\infty}, & \phi(\eta) = \dfrac{C - C_\infty}{C_\infty} \\ \Rightarrow T = T_\infty + (T_f - T_\infty)\theta(\eta) & & \Rightarrow C = C_\infty + C_\infty \phi(\eta) \end{array}\right\} \tag{7}$$

These are the ODEs that result due to diminution of the PDEs.

$$F'''(\eta) = \frac{1}{(1-\alpha\theta)} \left(\begin{array}{c} \beta(1-\alpha\theta) F'(\eta) + \alpha F''(\eta)\theta'(\eta) + \\ B_1 B_2 \left(\begin{array}{c} F'^2(\eta) - G^2(\eta) - \\ 2F(\eta) F''(\eta) + Fr F'^2(\eta) \end{array} \right) - B_1 H a e^{\gamma\eta} \end{array} \right), \tag{8}$$

$$G^{''}(\eta) = \frac{1}{(1-\alpha\theta)} \left(\begin{array}{c} \alpha\theta'(\eta) G^{'}(\eta) + \beta(1-\alpha\theta) G(\eta) + \\ B_1 B_2 \left(2F'(\eta) G(\eta) - 2F(\eta) G^{'}(\eta) + Fr G^2(\eta) \right) - B_1 H a e^{\gamma\eta} \end{array} \right),$$

$$\theta^{''}(\eta) = \frac{1}{(1.333Rd + B_4(1+\beta\theta))} \left(\begin{array}{c} -2B_3 \Pr F(\eta)\theta'(\eta) - B_4 \beta \theta^{'2}(\eta) \\ -BrHae^{\gamma\eta} \left(F^{'}(\eta) + G(\eta) \right) - \\ \frac{Br}{B_1} \left(F^{''2}(\eta) + G^{'2}(\eta) \right) \\ -B_3 \Pr \left(N_b \theta^{'}(\eta) \phi^{'}(\eta) + N_t \theta^{'2}(\eta) \right) \end{array} \right), \tag{9}$$

$$\phi^{''}(\eta) + \frac{N_t}{N_b} \theta^{''}(\eta) - KrSc\phi(\eta) + 2ScF(\eta)\phi^{'}(\eta) = 0. \tag{10}$$

The boundary conditions associated with these ODE's are as follows,

$$\left.\begin{array}{l} F^{'}(\eta) \to 0, \quad G(\eta) \to 0, \quad \theta(\eta) \to 0, \quad \phi(\eta) \to 0, \qquad \text{as} \quad \eta \to \infty \\ F^{'}(\eta) = \lambda, \quad F(\eta) = 0, \quad G(\eta) = 1, \quad B_4 \theta^{'}(\eta) + Bi(1 - \theta(\eta)) = 0, \\ \phi^{'}(\eta) + \dfrac{Nt}{Nb} \theta^{'}(\eta) = 0, \qquad \text{at} \quad \eta = 0. \end{array}\right\} \tag{11}$$

The parameters like porosity parameter, Brownian motion parameter, chemical reaction parameter, Hartmann number, Eckert number, Darcy-Forchheimer parameter, Schmidt number, radiation parameter, Prandtl number, width parameter, Brinkman number, thermophoresis parameter, that are not dimensional and utilized in the calculated ordinary differential equations are defined as,

$$B_1 = \frac{\mu_f}{\mu_{hnf}}, \quad \beta = \frac{\nu_f}{\omega k_\circ}, \quad Fr = \frac{C_b}{\sqrt{k_\circ}}, \quad Ha = \frac{\pi}{8}\frac{j_\circ M_\circ}{r\omega^2\rho_f}, \quad Rd = \frac{4\sigma^* T_\infty^3}{k^* k_f},$$
$$B_2 = \frac{\rho_{hnf}}{\rho_f}, \quad Pr = \frac{\nu_f \left(\rho c_p\right)_f}{k_f}, \quad Br = PrEc, \quad Ec = \frac{r^2\omega^2}{\left(c_p\right)_f \left(T_f - T_\infty\right)},$$
$$B_3 = \frac{\left(\rho c_p\right)_{hnf}}{\left(\rho c_p\right)_f}, \quad \gamma = -\frac{\pi}{a_\circ\sqrt{\frac{\omega}{\nu_f}}}, \quad N_b = \frac{\tau D_B C_\infty}{\nu_f}, \quad N_t = \frac{\tau D_T \left(T_f - T_\infty\right)}{T_\infty \nu_f},$$
$$B_4 = \frac{k_{hnf}}{k_f}, \quad Sc = \frac{\nu_f}{D_B}, \quad Kr = \frac{kr^2}{\omega}, \quad B_5 = \frac{\sigma_{hnf}}{\sigma_f}.$$

Important physical factors like the skin friction coefficient and the rates of mass and heat transport are also examined in this study. The pursuing are the mathematical formulations of the Sherwood number, Nusselt number and skin friction coefficient.

$$Nu_x = \frac{r\left(q_w + q_r\right)}{k_f\left(T_f - T_\infty\right)}, \quad C_f = \frac{\sqrt{\tau_W^2 + \tau_V^2}}{\rho_f U_W^2}, \quad Sh_x = \frac{r m_w}{\rho_f D_B C_\infty}. \tag{12}$$

The mass flux is indicated by m_w, the tangential shear stress is indicated by τ_θ, the radial shear stress is indicated by τ_ω, and the overall heat flux is represented by $(q_w + q_r)$. The following is a definition of these quantities:

$$q_w = -k_{hnf}\left(\frac{\partial T}{\partial z}\right)_{z=0}, \quad q_r = -\frac{4.33 T_\infty^3 \sigma^*}{k^*}\left(\frac{\partial T}{\partial z}\right)_{z=0}, \tau_W = \mu_{hnf}\left(\frac{\partial W}{\partial z}\right)_{z=0}, \tag{13}$$
$$\tau_V = \mu_{hnf}\left(\frac{\partial V}{\partial z}\right)_{z=0}, \quad m_w = -\rho_f D_B\left(\frac{\partial C}{\partial z}\right)_{z=0}, \quad Re_x = \frac{rU_W}{\upsilon_f} \text{ (Reynold's number)} \tag{14}$$

The dimensionless form of the Sherwood number, Nusselt number and skin friction coefficient.

$$\begin{aligned} Nu_x Re_x^{-\frac{1}{2}} &= -\left(\frac{k_{hnf}}{k_f} + 1.33Rd\right)\theta'(0), \\ C_f Re^{\frac{1}{2}} &= \frac{\mu_{hnf}}{\mu_f}\sqrt{F''^2(0) + G'^2(0)}, \\ Sh_x Re^{-\frac{1}{2}} &= -\phi'(0). \end{aligned}$$

2.1 Sensitivity analysis formulation

A local sensitivity analysis is carried out for the Nusselt number, skin friction and Sherwood number in order to quantitatively evaluate the relative impact of controlling physical factors on the transport characteristics. For a generic parameter p, the sensitivity coefficient is defined as $S_p^R = \frac{p}{R}\frac{\partial R}{\partial p}$, where the parameter R represents the response quantity of interest (Nu, Cf, *or* Sh), S_p^R denotes the normalized sensitivity coefficient. This formulation provides a dimensionless measure of the relative variation in the output response due to perturbations in the governing parameter. The sensitivity derivatives were numerically estimated using a second-order central finite difference

technique provided by as analytical evaluation of the derivatives is typically challenging for highly nonlinear couples systems.

$$\frac{\partial R}{\partial p} \approx \frac{R\left(p+\Delta p\right)-R\left(p-\Delta p\right)}{2\Delta p}$$

where a minor perturbation given to the appropriate parameter is indicated by Δp. To guarantee numerical stability and precise sensitivity estimates, a perturbation size of 1% for the baseline parameter value was used in the current simulations. A negative sensitivity coefficient denotes an inverse link, whereas a positive coefficient shows that the response variable rises with increasing parameter size. Additionally, the relative dominance of the associated physical process is quantified by the absolute value of the sensitivity coefficient.

Based on the calculated sensitivity coefficients, tornado diagrams were created to aid in visual comprehension and parameter ranking. Heat transfer, momentum transport, and mass diffusion are all impacted by dominant and insignificant transport processes, which are represented hierarchically in these diagrams.

3 Solution methodology

In this work, the bvp4c approach is used in solving the set of ODE's with a given bound scheme. The bvp4c function is an in-built solver of MATLAB which calculates the solution of boundary value problems for ODE's. The sensitivity framework was implemented through repeated perturbation-based numerical simulations using MATLAB bvp4c In order to apply this approach, initially, the commanding equations are transformed into a set of first-order ODEs., as defined in earlier sections. The differential equations mentioned above will now be rewritten as a first-order system using the following notations.

$$F\left(\eta\right)=y_1,\, F^{'}\left(\eta\right)=y_1^{'}=y_2,\, F^{''}\left(\eta\right)=y_2^{'}=y_3,\, F^{'''}\left(\eta\right)=y_3^{'},,$$

$$G\left(\eta\right)=y_4,G^{'}\left(\eta\right)=y_4^{'}=y_5,\, G^{''}\left(\eta\right)=y_5^{'},\,,$$

$$\theta\left(\eta\right)=y_6,\, \theta^{'}\left(\eta\right)=y_6^{'}=y_7,\, \theta^{''}\left(\eta\right)=y_7^{'},,$$

$$\phi\left(\eta\right)=y_8,\, \phi^{'}\left(\eta\right)=y_8^{'}=y_9,\, \phi^{''}\left(\eta\right)=y_9^{'},,$$

$\phi_{Al_2O_3}$	ϕ_{Ag}	Present	Wahid [38]	Turkyilmazoglu [39]
0.00	0.0	0.93387762	0.933877577	0.93387794
0.05	0.0	0.87642646	0.876426508	0.87642685
0.10	0.0	0.82186958	0.821869579	0.82186995
0.15	0.0	0.77012717	0.770127169	0.77012763
0.20	0.0	0.72103477	0.721034766	0.72103541

Table 2: Comparison in limiting case with published articles

This causes the problem to take the following shape.

$$
\begin{aligned}
y_1^{'} &= y_2, \\
y_2^{'} &= y_3, \\
y_3^{'} &= \frac{1}{(1-\alpha y_6)} \begin{pmatrix} \beta\left(1-\alpha y_6\right) y_2 + \alpha y_3 y_7 \\ +B_1 B_2\left(y_2^2 - y_4^2 - 2y_1 y_3 + F r y_2^2\right) - B_1 H a e^{\gamma \eta} \end{pmatrix}, \\
y_4^{'} &= y_5, \\
y_5^{'} &= \frac{1}{(1-\alpha y_6)} \begin{pmatrix} \alpha y_7 y_5 + \beta\left(1-\alpha y_6\right) y_4 \\ +B_1 B_2\left(2y_2 y_4 - 2y_1 y_5 + F r y_4^2\right) - B_1 H a e^{\gamma \eta} \end{pmatrix}, \\
y_6^{'} &= y_7, \\
y_7^{'} &= \frac{1}{(1.333Rd + B_4\left(1+\beta y_6\right))} \begin{pmatrix} -2B_3 \Pr y_1 y_7 - B_4 \beta y_7^2 \\ -BrHae^{\gamma\eta}\left(y_2 + y_4\right) - \frac{Br}{B_1}\left(y_3^2 + y_5^2\right) \\ -B_3 \Pr\left(N_b y_7 y_9 + N_t y_7^2\right) \end{pmatrix}, \\
y_8^{'} &= y_9, \\
y_9^{'} &= KrScy_8 - 2Scy_1 y_9 - \frac{N_t}{N_b}\left(y_7^{'}\right),
\end{aligned}
$$

Table 2 highlight the comparison of different values of Al_2O_3 nanoparticles while keeping other parameters fixed. Its shows an excellent agreement of the numerical values, which strengthes the validity of our methodology.

4 Results and discussions

The Nusselt number Nu, skin friction coefficient Cf and Sherwood number Sh are three important regulating parameters whose effects on the heat transport characteristics have been quantified through a thorough sensitivity analysis. The associated tornado diagrams provide additional visualization of the data, which are methodically summed in the sensitivity coefficient table. Both a quantitative ranking as shown in Table 3 and a physical understanding of parameter effects are provided by this integrated representation.

With a sensitivity value of 0.9044, the Biot number Bi is shown to have the greatest impact on the Nusselt number, suggesting that convective surface heat transport significantly controls the system's thermal performance as displayed in Figure 3(a) . The radiation parameter Rd (0.2343)

Parameters	Nu	Cf	Sh
Pr	0.15159961	-0.00325566	0.15159993
Rd	0.23429522	-0.00011997	-0.0040278
Nb	-6.2459387e-10	-6.07811470e-11	-1.0001000
Nt	-0.0007352	1.476550138e-05	0.99926474
Bi	0.90443027	0.003685312	0.90443042
Ha	0.00517735	-0.03688338	0.00517742

Table 3: Quantitative sensitivity analysis of governing parameters on thermal, momentum, and mass transport characteristics, represented by the Nusselt number, skin friction coefficient and Sherwood number, respectively.

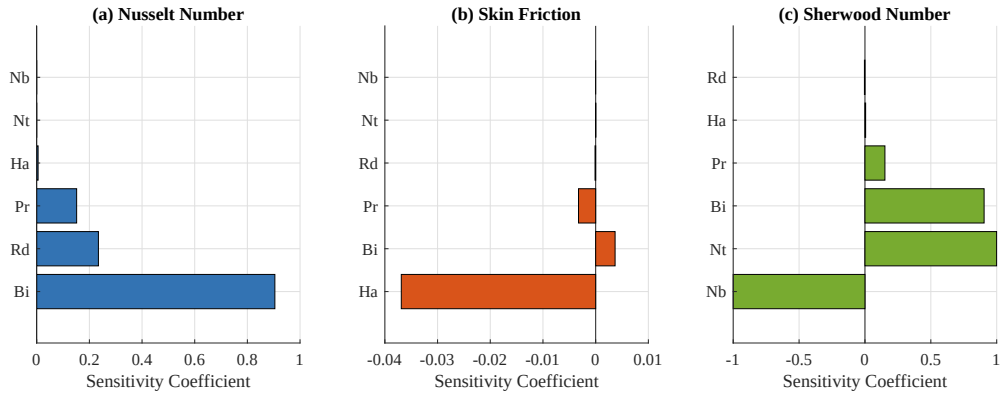


Figure 3: Visualization of parametric sensitivity

and the Prandtl number Pr (0.1516), which both make positive but noticeably smaller contributions, come next. On the other hand, Brownian motion Nb and practically minor in the current parameter regime, while magnetic parameter Ha and thermophoretic parameter Nt have minimal impact. This order is well supported by the accompanying tornado chart, which shows Bi as the most important element, followed by Rd, and Pr, with the remaining factors making very minor contributions.

A distinct pattern is seen in Figure 3(b) for the skin friction coefficient Cf. Because of Lorentz force-induced flow resistance, magnetic effects tend to diminish wall shear stress, as seen by the magnetic parameter $Hs's$ considerable negative sensitivity (-0.0369). The remaining factors have relatively little effect on Cf, indicating that under the current circumstances, momentum transmission close to the wall is less susceptible to heat and nanoparticle-related effects.

The Brownian motion parameter Nb and the thermophoresis parameter Nt, which have almost opposing effects, have the greatest impact on the Sherwood number Sh represented in Figure 3(c). There is a clear conflict between diffusive and thermophoretic processes in nanoparticle transport, as evidenced by the fact that Nt greatly increases mass transfer (0.9993) while Nb dramatically reduces it (-1.0001). The features of mass transfer are little affected by other factors, such as Pr, Bi, and Ha.

Overall, the combined sensitivity table and tornado visualization show that while mass transfer is heavily influenced by nanoparticle transport mechanisms (Brownian motion and thermophoresis), heat transfer is mainly controlled by thermal boundary conditions through the Biot number. Magnetic effects, on the other hand, are secondary and mainly affect momentum transmission rather than mass or heat diffusion. These discoveries greatly improve the interpretability and robustness of the current model and offer a distinct physical hierarchy of regulating factors.

Fig. 4 depicts the impact of the permeability variable β on the radial velocity $F'(\eta)$. It is noticed that with greater values of β, the dimensionless radial velocity diminishes. In this case, a greater β denotes a highly permeable medium, which introduces flow disturbances, and consequently, a decline in radial velocity is observed. Furthermore, an increase in permeability enhances the effects of convective flow. This indicates that other processes like suction and Joule heating are less significant than the convective heat transfer. The robust effects of convection help in removing the fluid from the disk, which inhibits the fluid's radial motion toward the disk. Hence, the dimensionless radial velocity $F'(\eta)$ reduces. Fig. 5 illustrates the outcomes of permeability parameter β on tangential velocity $G(\eta)$. The dimensionless $G(\eta)$ decreases with increasing β. This decrease in velocity can be explained by the increasing dominance of convective effects; as the porous medium's permeability increases, convective effects become more pronounced. The greater convective transport moves the fluid more efficiently away from the disk, carrying fluid away from the disk. The axial flow is reduced, this causes a reduction in the tangential velocity. Fig. 6 shows the $\theta(\eta)$ variation with porosity parameter β. Temperature increases with a boost in porosity parameter β. That is, increased porosity β implies that the fluid passes through a more open or porous material. This enables the small particles (nanofluids) of the fluid to pass more freely and collide more frequently. These frequent collisions produce more heat, and due to this, the fluid's temperature profile $\theta(\eta)$ escalates. The porosity parameter's β's effect on the concentration profile $\phi(\eta)$ is depicted in the Fig. 7. The concentration profile $\phi(\eta)$ becomes increasing as the porosity rises. This happens because increased diffusion through the medium is necessary due to higher porosity, which provides less resistance to solute movement. Fig. 8

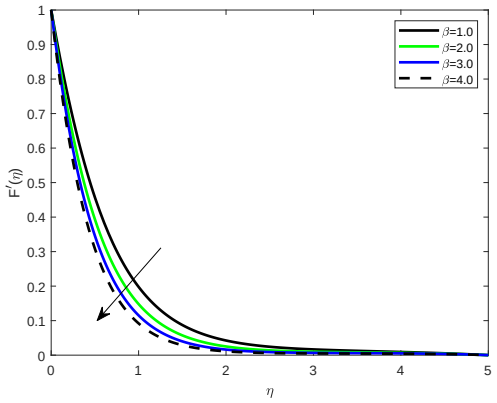


Figure 4: Fluctuation in $F'(\eta)$ contrary to β

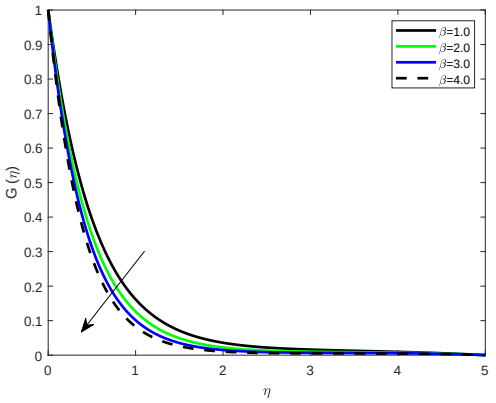


Figure 5: Fluctuation in $G(\eta)$ contrary to β

displays how $F'(\eta)$ is affected by Fr. The radial velocity $F'(\eta)$ is seen to decrease when the

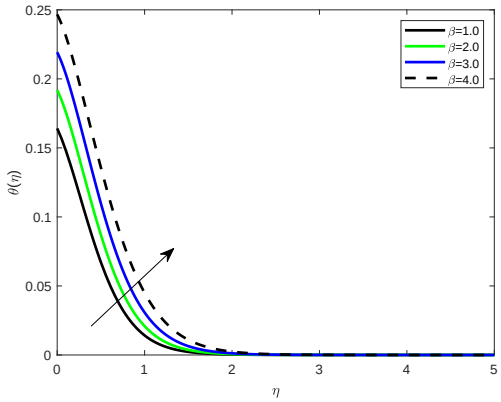


Figure 6: Fluctuation in $\theta(\eta)$ contrary to β

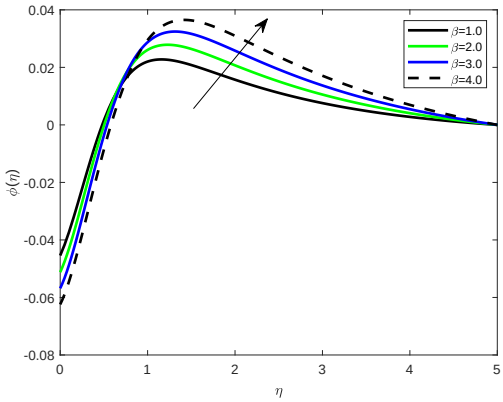


Figure 7: Fluctuation in $\phi(\eta)$ contrary to β

Darcy-Forchheimer parameter increases. This happens because fluid motion is slowed down by greater Darcy-Forchheimer Fr values, which increase flow resistance through increased drag forces. The impact of different Hartmann numbers Ha values on the radial $F'(\eta)$ for hybrid nanofluid is shown in Fig. 9. Plotting the non-dimensional distribution against $F'(\eta)$ indicates that the radial velocity rises noticeably as the Hartmann number Ha boosts. A non-dimensional metric called Ha contrasts the impact of magnetic and viscous forces. Fig. 10 exhibits how $F'(\eta)$

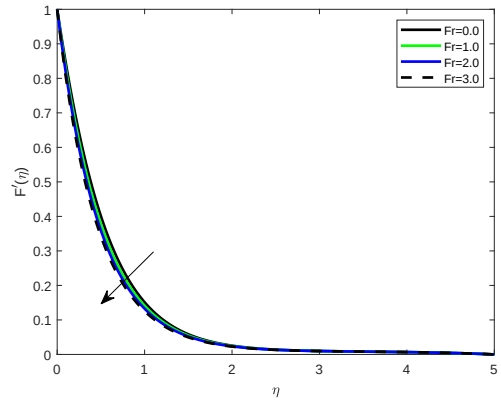


Figure 8: Fluctuation in $F'(\eta)$ contrary to Fr

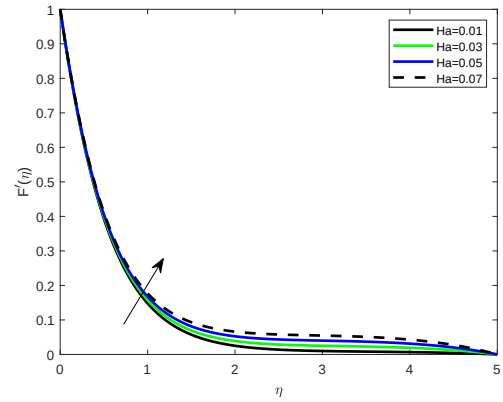


Figure 9: Fluctuation in $F'(\eta)$ contrary to Ha

is affected by width parameter γ. The image makes it clear that $F'(\eta)$ rises as γ does. This phenomenon arises because a larger width encourages stronger radial flow by giving the fluid more room to spread outward. The fluid is less constrained and can accelerate radially as the available area for flow increases. Consequently, an increase in radial velocity is a natural consequence of the rise in the width variable γ. The impact of the chemical reaction parameter Kr on $\phi(\eta)$ is depicted in the Fig. 11. The concentration profile $\phi(\eta)$ steadily drops as Kr rises. The equilibrium between transport and reaction processes is upset when Kr increases because it speeds up reactant consumption. A declining concentration $\phi(\eta)$ is the result of the concentration levels being lowered by this quick reaction rate. The impact of the Brinkman number Br on the temperature $\theta(\eta)$

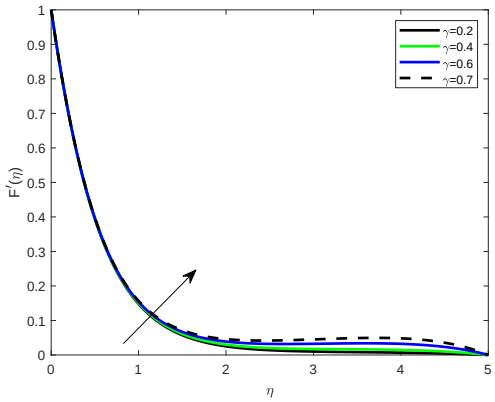


Figure 10: Fluctuation in $F'(\eta)$ contrary to γ

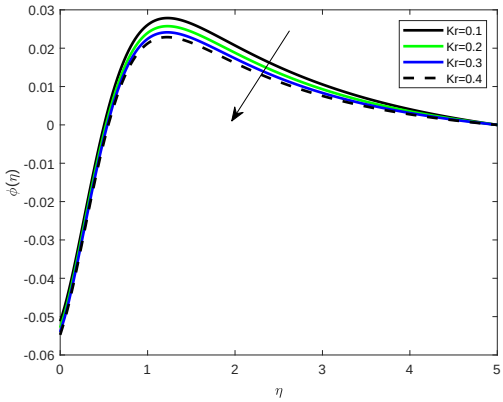


Figure 11: Fluctuation in $\phi(\eta)$ contrary to Kr

and concentration $\phi(\eta)$ profiles are portrayed in the Figs. 12 and 13. It has been noted that both characteristics noticeably increase when the Brinkman number Br does. Stronger viscous dissipation results in more internal heat generation in the fluid, as shown by a higher Brinkman number Br. The temperature profile $\theta(\eta)$ rises as a result of this additional heat. The fluid's characteristics alter in reaction to the increased thermal energy, slowing down particle mobility and improving solute retention close to the boundary layer. Consequently, a thicker concentration profile $\phi(\eta)$ is produced as the solute particle concentration rises. As a result, greater Brinkman numbers Br raise the flow field's $\theta(\eta)$ and $\phi(\eta)$ levels.

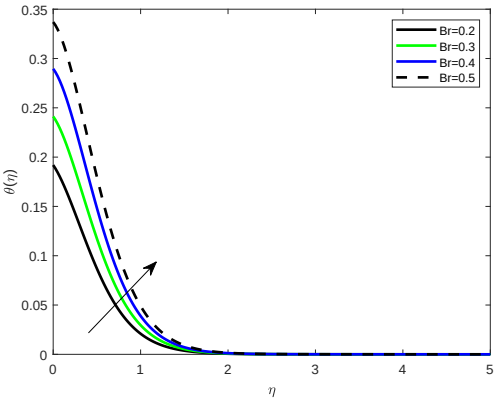


Figure 12: Fluctuation in $\theta(\eta)$ contrary to Br

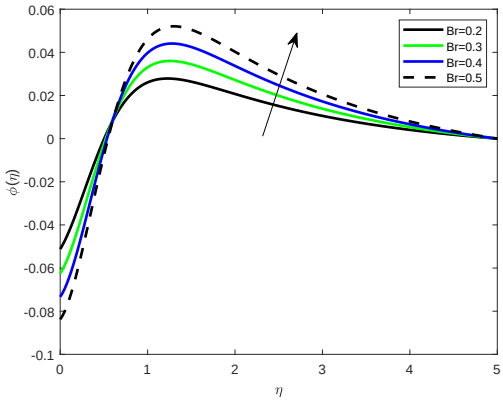


Figure 13: Fluctuation in $\phi(\eta)$ contrary to Br

The effects of different volume fractions of aluminium oxide (ϕ_1) and silver (ϕ_2) nanoparticles on $\theta(\eta)$ are depicted in Figs. 14 and 15 respectively. The nanoparticles interact more strongly, increasing the nanofluid's effective viscosity. The fluid's ability to retain heat is improved by the increased thermal conductivity brought on by the higher concentration of nanoparticles. Consequently, the dimensionless temperature of the nanofluid is greater, indicating a more efficient thermal energy distribution in the system.

The impact of injection and suction λ settings on the tangential velocity profile $G(\eta)$ is shown

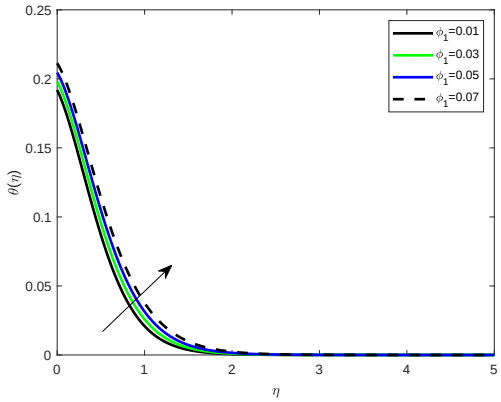


Figure 14: Fluctuation in $\theta(\eta)$ contrary to ϕ_1

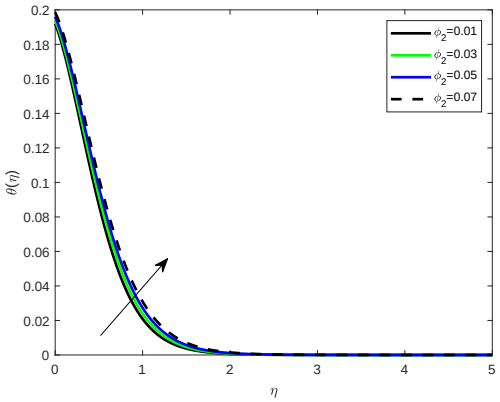


Figure 15: Fluctuation in $\theta(\eta)$ contrary to ϕ_2

in Fig. 16. It has been found that tangential velocity $G(\eta)$ decreases as these values rise. This decrease is explained by the fact that both injection and suction disrupt the fluid's rotating motion. While injection adds a normal component of velocity that upsets the rotational flow structure, suction thins the boundary layer and suppresses the tangential momentum close to the surface. Consequently, as suction and injection strength increase, the total tangential velocity $G(\eta)$ inside the boundary layer decreases. Fig. 17 shows how $F'(\eta)$ is affected by the viscosity-variation variable α. It is clear that $F'(\eta)$ declines as the viscosity-variation parameter α rises. This behavior results from higher viscosity, which inhibits flow in the radial direction by increasing resistance to fluid motion. The radial momentum decreases as the viscous forces gain strength, resulting in a slower velocity inside the boundary layer.

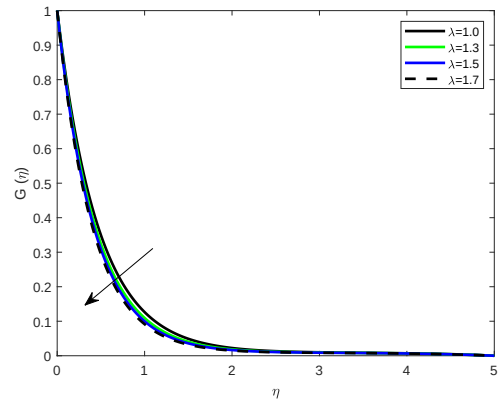


Figure 16: Fluctuation in $G(\eta)$ contrary to λ

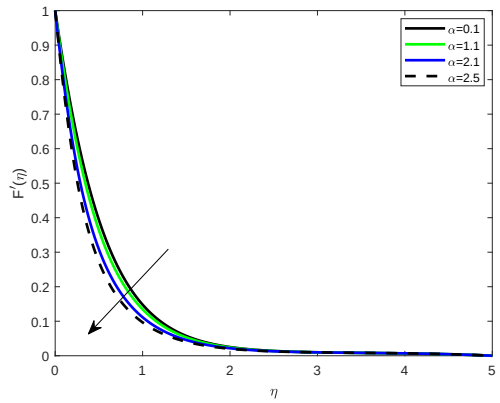


Figure 17: Fluctuation in $F'(\eta)$ contrary to α

The pumping/suction parameter λ varying from 1.0 to 2.5 enhances Cf nonlinearly giving the impression of deep concentration needed for imposition, concurrently declining both Nu and Sh caused by boundary layer depletion. Increasing Bi from 0.2 to 0.5 gives rise to stronger surface convection, increasing Cf and Nu while making Sh more negative. The increase in Rd was altered from 0.3 to 0.6 which increased Nu due to more radiation aiding heat transfer but made little

λ	Bi	Rd	Pr	Br	Nb	Cf	Nu	Sh
1.1						2.9966118	0.2141932	-0.0650795
1.2						3.2183266	0.2131949	-0.0647762
1.3						3.4521317	0.2118811	-0.0643770
	0.3					3.0020743	0.3060532	-0.0929898
	0.4					3.0072439	0.3886381	-0.1180821
	0.5					3.0121045	0.4627393	-0.1405966
		0.4				2.9965032	0.2311697	-0.0649854
		0.5				2.9964188	0.2480702	-0.0648846
		0.6				2.9963548	0.2648943	-0.0647781
			6.3			2.9964549	0.2147135	-0.0652376
			6.4			2.9963015	0.2152202	-0.0653915
			6.5			2.9961513	0.2157138	-0.0655415
				0.3		3.0020447	0.2009062	-0.0610424
				0.4		3.0073039	0.1878990	-0.0570904
				0.5		3.0124125	0.1751406	-0.0532139
					0.5	2.9966118	0.2141932	-0.0520636
					0.6	2.9966118	0.2141932	-0.0433863
					0.7	2.9966118	0.2141932	-0.0371883

Table 4: Variation in skin friction, Sherwood and Nusselt number against λ, Bi, Rd, Pr, Br, Nb

change to Cf and Sh. The Prandtl number Pr also contributes to boost in Nu, altering from 6.2 to 6.5, but makes Sh decrease due to relaxation in thermal diffusion. The increase of Nb from 0.4 to 0.7 decreases Nu and Sh since randomness brought forth by the nanoparticle reduces the heat and mass gradient.

5 Concluding remarks

The study examines the flow of a hybrid nanofluid, $(Ag - Al_2O_3/H_2O)$, over a spinning and stretchy disk under various physical conditions. These consist of thermal radiation, chemical reactions, viscous dissipation, external magnetic fields, Riga surface effects, and Joule heating effects. Thermal conductivity and temperature-dependent viscosity are included in the study, along with a zero mass flow condition and a convective boundary condition for temperature for species concentration. A comprehensive sensitivity analysis has been carried out to quantify the influence of key controlling parameters on the thermal transport characteristics. The results are systematically summarized in the sensitivity coefficient table and further visualized through the corresponding tornado diagrams. The main findings are as follows.

- Stronger convective effects and frictional heating cause increased permeability and flow resistance via β and Fr to increase temperature and concentration while generally decreasing fluid velocities.
- In this particular flow configuration, the magnetic field intensity Hartmann number Ha atypically raises tangential and radial velocities while simultaneously encouraging the buildup of heat and solute.
- The present investigation demonstrates that the thermal transport characteristics of the hybrid nanofluid system are strongly governed by the Biot number, whereas Brownian motion and thermophoretic mechanisms predominantly control the mass transfer behavior.
- The incorporation of perturbation-based sensitivity coefficients and tornado diagram visualization significantly enhances the physical interpretability of the nonlinear transport system compared to convenctional profile-based analysis.
- Higher chemical reaction rates Kr and Brownian motion parameters Nb lead to thinner concentration boundary layers, which in turn reduce solute concentrations.
- The combined numerical and sensitivity-driven methodology presented in this study offers a robust computational platform for advanced hybrid nanofluid transport analysis and may serve as a useful benchmark for future investigations involving nonlinear thermal systems, porous media transport, and magnetohydrodynamic flow applications.
- Due to limited convective transport, viscosity change α raises temperature and concentration while decreasing velocities.

Acknowledgement Acknowledgment: The work was supported and funded by the Deanship of Scientific Research at Imam Mohammad Ibn Saud Islamic University (IMSIU) (grant number

IMSIU-DDRSP2603).

References

[1] Th. V. Karman. Uber laminare und turbulente Reibung. *ZAMM- J. App. Math. Mech.*, 1(4):233–252, 1921.

[2] R. Berker. A new solution of the Navier-Stokes equation for the motion of a fluid contained between two parallel plates rotating about the same axis. *Arch. Mech. Stos.*, 31:265–280, 1979.

[3] R. Berker. An exact solution of the Navier-Stokes equation: the vortex with curvilinear axis. *Int. J. Eng. Sci.*, 20:217–230, 1982.

[4] C. S. K. Raju, S. U. Mamatha, P. Rajadurai, and I. Khan. Nonlinear mixed thermal convective flow over a rotating disk in suspension of magnesium oxide nanoparticles with water and EG. *Eur. Phys. J. Plus.*, 134(5):196, 2019.

[5] U. T. Bodewadt. Die Drehstromunguberfestem Grund. *Z. Angew Math. Mech.*, 20:241–252, 1940.

[6] E. Ragupathi, D. Prakash, M. Muthtamilselvan, and Q. M. Al-Mdallal. Dynamics of Non-Newtonian methanol monveying aluminium alloy over a rotating disc: Consideration of variable nanoparticle radius and inter-particle spacing. *Z. Angew Math. Mech.*, 35(28):285402, 2024.

[7] T. Mehmood, M. Ramzan, and F. Howari et al. Application of response surface methodology on the nanofluid flow over a rotating disk with autocatalytic chemical reaction and entropy generation optimization. *Sci. Rep.*, 11(1):1–18, 2021.

[8] H. Chen and S. R. Patel. Experimental validation of numerical models for radially stretchable porous rotating disks: deformation and porous property characterization. *J. Fluids Eng.*, 143(7):71205, 2021.

[9] K. Taghavi. Analysis of direct-contact melting under rotation. *J. Heat Trans.*, 112:137–143, 1990.

[10] Attia and A. Hazem. Rotating disk flow and heat transfer of a conducting non-Newtonian fluid with suction-injection and Ohmic heating. *J. Brazilian Soc. Mech. Sci. Engr.*, 29:168–173, 2007.

[11] M. M. Rashidi, S. A. M. Pour, T. Hayat, and S. Obaidat. Analytic approximate solutions for steady flow over a rotating disk in porous medium with heat transfer by homotopy analysis method. *Comput. FLUIDS*, 54:1–9, 2012.

[12] CattaneoChristov heat flux model in DarcyForchheimer radiative flow of MoS_2SiO_2.

[13] M. Ramzan, T. Mehmood, H. Alotaibi, H. A. S. Ghazwani, and T. Muhammad. Comparative study of hybrid and nanofluid flows amidst two rotating disks with thermal stratification: statistical and numerical approaches. *Case Stud. Therm. Eng.*, 28:101596, 2021.

[14] P. Ram, V. Kumar, and S. Sharma. Magneto-viscous effects on unsteady nano-ferrofluid flow influenced by low oscillating magnetic field in the presence of rotating disk. *Res. Adv. Fluid Mech. Ther. Engr.*, pages 89–97, 2014.

[15] N. Acharya, R. Bag, and P. K. Kundu. Influence of Hall current on radiative nanofluid flow over a spinning disk: a hybrid approach. *Phys. E: low-Dimens. Sys. Nanostruc.*, 111:103112, 2019.

[16] M. R. A. Rahman, K. Y. Leong, A. C. Idris, M. R. Saad, and M. Anwar. Numerical analysis of the forced convective heat transfer on $Al_2O_3 - Cu$/water hybrid nanofluid. *Heat Mass Transf.*, 53:1835–1842, 2017.

[17] S. Ahmad, K. Ali, and M. Rizwan et al. Heat and mass transfer attributes of copper-aluminum oxide hybrid nanoparticles flow through a porous medium. *Case Stud Thermal Eng.*, 25:100932, 2021.

[18] S. S. Ghadikolaei, Kh. Hosseinzadeh, and D. D. Ganji. Investigation on ethylene glycol-water mixture fluid suspend by hybrid nanoparticles ($TiO_2 - CuO$) over rotating cone with considering nanoparticles shape factor. *J. Mol. Liq.*, 272:226–236, 2018.

[19] E. Tayari, L. Torkzadeh, D. D. Ganji, and K. Nouri. Investigation of hybrid nanofluid SWCNT-MWCNT with the collocation method based on radial basis functions. *European Phys. J. Plus.*, 138(1):3, 2023.

[20] A. J. Chamkha, A. S. Dogonchi, and D. D. Ganji. Magneto-hydrodynamic flow and heat transfer of a hybrid nanofluid in a rotating system among two surfaces in the presence of thermal radiation and Joule heating. *AIP Adv.*, 9, 2019.

[21] R. Khan, R. H. Rasheed, A. Alizadeh, A. M. Sadeq, S. A. Hussein, N. S. Sawaran Singh, H. Rajab, and K. Hajlaoui. Combined hydrothermal and entropy generation analysis in a parabolic trough collector using a hybrid nanofluid and bent-plate vortex generators: a two-phase mixture model approach. *J Therm Anal Calorim*, 150:18607–18626, 2025.

[22] A. Shaheen, M. J. Hasan, M. Imran, H. Waqas, and T. Muhammad. Hydrothermal properties with entropy generation effects on a hybrid nanofluid considering thermal radiation on a stretching/shrinking sheet. *Num. Heat Trans., Part A: Appl.*, pages 1–22, 2024.

[23] A. Aworinde, S. O. Okuma, A. O. Areo, M. O. Akande, P. Adegbite, and A. O. Akindele. The effect of a Riga plate on Casson hybrid nanofluid flow along a stretching cylinder with an exponential heat source and thermal radiation. *J. Sci. Tech.*, 16(1):10–22, 2024.

[24] M. Ferdows, M. Shamshuddin, A. M. Rashad, M. G. Murtaza, and S. O. Salawu. Three-dimensional boundary layer flow and heat/mass transfer through stagnation point flow of hybrid nanofluid. *J. Engr. Appl. Sci.*, 71(57), 2024.

[25] T. Hayat, S. Qayyum, A. Alsaedi, and S. Asghar. Radiation effects on the mixed convection flow induced by an inclined stretching cylinder with non-uniform heat source/sink. *PLoS One.*, 12(4):e0175584, 2017.

[26] C. Mira and H. G. Chandra. The effects of variable viscosity and thermal conductivity on MHD flow due to a point sink. *Mat. Ensen. Univ*, 16(2):2128, 2008.

[27] M. Malik, M. Bibi, F. Khan, and T. Salahuddin. Numerical solution of Williamson fluid flow past a stretching cylinder and heat transfer with variable thermal conductivity and heat generation/absorption. *AIP Adv.*, 6:035101, 2016.

[28] M. I. Afridi, M. Qasim, and O. D. Makinde. Second law analysis of boundary layer flow with variable fluid properties. *J. Heat. Transf.*, 139(10):104505, 2017.

[29] G. Sowmya and B. J. Gireesha. Thermal stresses and efficiency analysis of a radial porous fin with radiation and variable thermal conductivity and internal heat generation. *J. Therm. Anal. Calorim.*, 147:4751–4762, 2022.

[30] M. Hamid, M. Usman, T. Zubair, R. U. Haq, and W. Wang. Shape effects of MoS2 nanoparticles on rotating flow of nanofluid along a stretching surface with variable thermal conductivity: A Galerkin approach. *Int. J. Heat Mass Transf.*, 124:706–714, 2018.

[31] I. Ahmad, S. Aziz, S. U. Khan, and N. Ali. Periodically moving surface in an Oldroyd-B fluid with variable thermal conductivity and Cattaneo-Christov heat flux features. *Heat Transf.*, pages 1–21, 2020.

[32] S. Lahmar, M. Kezzar, R. E. Mohamed, and M. R. Sari. Heat transfer of squeezing unsteady nanofluid flow under the effects of an inclined magnetic field and variable thermal conductivity. *Physica A Stat. Mech. Appl.*, 540:123138, 2020.

[33] F. Sultan, W. Khan, M. Shahzad, M. Ali, and Z. Hussain. Physical assessments on variable thermal conductivity and heat generation/absorption in cross magneto-flow model. *J. Therm. Anal. Calorim.*, 140:1069–1078, 2020.

[34] H. Waqas, A. Kafait, M. Alghamdi, T. Muhammad, and A. S. Alshomrani. Thermo-bioconvectional transport of magneto-casson nanofluid over a wedge containing motile microorganisms and variable thermal conductivity. *Alex. Engr. J.*, 2021.

[35] N. Abbas, W. Shatanawi, K. Abodayeh, and T. A.M. Shatnawi. Comparative analysis of unsteady flow of induced MHD radiative Sutterby fluid flow at nonlinear stretching cylinder/sheet: Variable thermal conductivity. *Alex. Engr. J.*, 72:451–461, 2023.

[36] B. K Sharma, P. Sharma, N. K. Mishra, and U. F. Gamiz. Darcy-forchheimer hybrid nanofluid flow over the rotating Riga disk in the presence of chemical reaction: Artificial neural network approach. *Alex. Engr. J.*, 76:101–130, 2023.

[37] M. Bilal, T. Ishfaq, S. Ahmad, and Y. Mehmood. A numerical simulation of the unsteady mhd nanofluid flow over a rotating disk in a porous medium with uniform suction and convective effects. *Int. J. Ambient Energy*, 45(1), 2024.

[38] N. S. Wahid, N. Md.Arifin, N. S. Khashiie, and I. Pop. Unsteady $al_2o_3 - cu/h_2o$ hybrid nanofluid flow over a rotatable stretching disk with heat generation and deceleration: Stable dual solutions. *Num. Heat Trans., Part A: Appl.*, 86(7):1951–1967, 2023.

[39] M. Turkyilmazoglu. MHD fluid flow and heat transfer due to a stretching rotating disk. *Int. J. Therm. Sci.*, 51:195201, 2012.